Variability of the Sub-Antarctic Mode Water subduction rate during the Argo period

Tangdong Qu, [1] Shan Gao, [2, 3, 4] and Rana A. Fine [5]

[1] Joint Institute for Regional Earth System Science and Engineering, University of California, Los Angeles, CA

[2] Institute of Oceanology, Chinese Academy of Sciences, Qingdao, China

[3] Center for Ocean Mega-Science, Chinese Academy of Sciences, Qingdao, China

[4] Laboratory for Ocean Dynamics and Climate, Pilot National Laboratory for Marine Science and Technology, Qingdao, China

[5] Rosenstiel School of Marine and Atmospheric Science, University of Miami, Miami, FL

Key Points:

1. A quasi-biennial variability in the Sub-Antarctic Mode Water subduction rate is revealed in response to the mixed layer depth variability;
2. The Sub-Antarctic Mode Water subduction rate has increased, contributing to the water's volume increase during the Argo period;
3. Changes in wind stress curl associated with the westerly winds play a key role in modulating the Sub-Antarctic Mode Water subduction rate.

(Submitted to *Geophysical Research Letter* on 01/27/20 and accepted for publication on 06/09/20)

Corresponding Author Address: Dr. Tangdong Qu, Joint Institute for Regional Earth System Science and Engineering, University of California at Los Angeles, 607 Charles E. Young Drive East, Los Angeles, CA 90095, Email: tangdong@ucla.edu

Abstract

Both a quasi-biennial variability and an overall linearly increasing trend are identified in the Sub-Antarctic Mode Water (SAMW) subduction rate across the southern hemisphere ocean, using the Argo data during 2005-2019. The quasi-biennial variability is mainly due to variability of the mixed layer depth. Variability of wind stress curl in the SAMW formation regions associated with the Southern Annular Mode plays a critical role in generating the quasi-biennial variability of the mixed layer depth and consequently the SAMW subduction rates. The SAMW subduction rate across the southern hemisphere ocean, long-term mean totaling 56 Sv, has increased at 0.73±0.65 Sv yr^{-1} over the past 15 years. The increase has directly contributed to the observed increase in the total SAMW volume. Much of this increasing trend can be explained by the deepening mixed layers, which in turn are primarily forced by the strengthening westerly winds under an increasing Southern Annular Mode.

Plain Language Summary

The upper ocean heat content has increased globally during the past decades. Recent studies have shown that this warming trend has concentrated in the extra-tropical southern hemisphere ocean and can be largely explained by the Sub-Antarctic Mode Water (SAMW) variability. Analysis of the Argo data reveals an increasing trend of the SAMW subduction rate during the period 2005-2019. Superimposed with this increasing trend is a quasi-biennial variability resulting from changes of the mixed layer depth. The increasing trend of the SAMW subduction rate directly contributes to the decade-long increase of the total SAMW volume. A large portion of this increasing trend is due to deepening of the mixed layer. Enhanced downward Ekman pumping in the SAMW subduction regions associated with an increasing Southern Annular Mode is primarily responsible for the increasing trends of the mixed layer depth and consequently the SAMW subduction rate.

1. Introduction

Recent studies have shown that the upper ocean heat content has increased globally over the past decades (Gille, 2002; Roemmich et al., 2015; Llovel and Terray, 2016). This warming trend was particularly evident since 2005, when the upper ocean (0-2000 m) monitoring by Argo became available (Roemmich et al., 2015; Llovel and Terray, 2016). Analyses of the Argo data indicated that the observed upper ocean heat gain is not evenly distributed over the global ocean but especially pronounced in the mid- to high-latitude southern hemisphere ocean (e.g., Roemmich et al., 2015; Llovel and Terray, 2016; Sallee, 2018). A prominent water mass of the region, the Sub-Antarctic Mode Water (SAMW), is identified around the southern subtropical gyres as a layer of low potential vorticity (PV) acquired during its formation (McCartney, 1977). Variability of the SAMW properties on decadal and longer time scales has been reported by recent studies (e.g., Bindoff and McDougall 2000; Gille 2002; Bryden et al. 2003; Gao et al., 2018; Kolodziejczy et al., 2019; Portela et al., 2020). Among others, Gao et al. (2018) showed that the SAMW has significantly thickened, deepened, and warmed during the period from 2005 to 2015. These changes in the SAMW properties may explain up to 65% of the total heat gain in the upper 2,000 m of the extra-tropical southern hemisphere ocean between 30°S and 60°S. The subduction of the SAMW also opens a window of ventilation that takes up a significant amount of climatically important gases, such as CO_2 and chlorofluorocarbons (e.g., Sabine et al. 2004; Willey et al. 2004; Hartin et al., 2011). For all these reasons, study of the SAMW has become a topic of interest.

Subduction of the SAMW occurs to the north of the Sub-Antarctic Front (SAF) (Orsi et al, 1995) at various locations. Ekman fluxes of the Antarctic surface water, winter cooling, and eddy diffusion generate convection that results in deep mixed layers (e.g., McCartney, 1977; Sallee et al., 2008; Holte et al., 2012). Once subducted, the SAMW spreads into the subtropical gyres and fills much of the southern hemisphere ocean at depths of the permanent thermocline (e.g., Hanawa and Talley, 2001). Some portion of this water mass returns to the Sub-Antarctic Zone in the southward-flowing western boundary currents, directly contributing to the inter-connected circulation system of the southern subtropical gyres, known as the Southern Hemisphere Super-Gyre, and potentially the Atlantic meridional overturning circulation (e.g., Fine, 1993; Speich et al., 2002; Ridgeway and Dunn, 2007; Roemmich, 2007; Qu et al., 2019).

A question that remains is what causes the observed variability in the SAMW properties. Since subduction is the only oceanic process that directly links the SAMW to surface forcing, it is hypothesized that much of the observed variability in the SAMW properties is due to changes in the SAMW subduction rate, though recent studies also emphasize the importance of diapycnal transformation from below (e.g., Portela et al, 2020). Increased ventilation in the southern subtropical gyres has been recognized by previous studies using tracer data and numerical models (e.g., McDonagh et al., 2005; Fine, 2011, Waugh et al., 2013; Tanhua et al., 2013; Wang et al., 2014; Talley et al., 2016; Fine et al., 2017), but variability of the SAMW subduction rate over the entire southern hemisphere ocean has not been carefully examined using in-situ observations. Here, we analyze the 15-year-long (2005-2019) time series of the Argo data to quantify variability of the SAMW subduction rate. The atmospheric and oceanic forcing of this variability is also examined.

2. Data and method of analysis

A large number of Argo floats have been deployed since the early 2000s, recording temperature and salinity of the ocean from a typical upper level of ~5 m to about 2000 m. Based on all Argo temperature and salinity profiles that have a “passed” flag, the Asian Pacific Data Research Center (APDRC) of the International Pacific Research Center, University of Hawaii, has created a near real-time, monthly temperature/salinity product of the global ocean on a 1°×1° grid. This data product (called the APDRC data product below) has a total of 26 (standard) vertical levels and spans from January 2005 to the present. Temperature and salinity profiles from the APDRC product for the period 2005-2019 over the southern hemisphere ocean between 10°S and 60°S are used for the present study. Also used for the present study is the NCEP/ NCAR re-analysis wind product (Kalnay et al., 1996). Additional information about these data and reanalysis products can be found on the web pages provided in the Acknowledgements.

The annual subduction rate, S_{ann}, is defined as the volume flux of mixed layer water entering the thermocline per unit horizontal area during a year (e.g., Woods, 1985; Williams et al., 1995). Following Qiu and Huang (1995), we release particles at the base of the winter (September) mixed layer at every grid point and track them in a Lagrangian framework for one year with a time interval of 5 days. According to their Eq. (5), S_{ann} can be expressed as

$$S_{ann} = -\overline{\left(w_{ek} - \frac{\beta}{f}\int_{-h_m}^{0} v dz\right)} + \frac{1}{T}\left(h_m(t_1) - h_m(t_2)\right), \tag{1}$$

where h_m is the mixed layer depth (MLD), w_{ek} is the Ekman pumping velocity, v is the meridional velocity, f is the planetary vorticity, β is the gradient of the planetary vorticity, t_1 and t_2 are the end of the first and second winter, respectively, and T is 1 year, representing the time period between t_2 and t_1. The first term on the right hand side of Eq. (1) is the contribution from vertical pumping, and the overbar indicates an average over the one-year trajectory. The second term is the difference of the MLD at locations of a particle separated in time by one year between the first and second winter, representing the contribution from lateral induction due to sloping of the mixed layer base (also see Huang and Qiu, 1998, and Qu et al., 2002). Due to data limitation, effects of mixing are ignored in this study.

The MLD is a key factor influencing S_{ann}. The criteria used to define the MLD have been diverse in literature (e.g., Kara et al., 2000; de Boyer Montegut et al., 2004). Following de Boyer Montegut et al. (2004), we define the MLD using a threshold value of density, $\Delta\sigma_\theta$=0.03 kg m^{-3}, from a near-surface value at 10 m depth, which is believed to provide optimal estimates of the MLD. To test the sensitivity of the MLD to its defining criteria, we also tried different temperature increments (e.g., 0.2°C, 0.5°C) using the density-based criteria (Lukas and Lindstrom,1991; Sprintall and Tomczak, 1992). These criteria yield essentially the same MLD patterns, except for some slight differences in its magnitude.

The gridded temperature and salinity from the APDRC data product are converted into dynamic height by assuming a level of no-motion at 2,000 db, from which geostrophic velocity is calculated. Analysis of these datasets provides the first observation-based estimate of the SAMW subduction rate for the period from 2005 to 2019.

3. Annual subduction rate and variability

Following earlier studies (McCartney, 1977; Hanawa and Talley, 2001; Gao et al., 2018), we define the SAMW as the water formed in the surface density range σ_0=26.5-27.1 kg m^{-3} north of the SAF (Orsi et al., 1995), where surface temperature and salinity are relatively low (Figs. 1a-b). In response to the strong westerly winds, vertical Ekman pumping in the Sub-Antarctic Zone is essentially downward (Fig. 1c), which together with surface cooling generate deep winter mixed layers over the region (Fig. 1d). Within the selected density range, the winter mixed layer is often deeper than 300 m, and sometimes reaches as deep as 500 m, providing a favorable condition for SAMW formation (e.g., Qu et al., 2008; Liu and Huang, 2012).

We calculate the SAMW annual subduction rate using the MLD and velocity fields from Argo (section 2). The 2005-2019 averaged annual subduction rate shows a large spatial variability (Fig. 2a). High subduction rates (>100 m yr^{-1}) are visible in all the three ocean basins, but most prominent in the eastern South Indian (south of Australia) and central to eastern South Pacific Oceans. Consistent with earlier studies (e.g., McCartney, 1977; Hanawa and Talley, 2001; Liu and Huang, 2012), high subduction rates extend southward as we progress eastward in the South Indian and Pacific Oceans. These high subduction rates coincide with large MLD gradients (Figure 1d), where differences are largest in the MLDs between the first and second winter on particle trajectories (Figure S1). In the South Atlantic, as compared with the other two oceans, the SAMW subduction rate is relatively low and its subduction region extends farther northward. Integrating over the entire southern hemisphere ocean between the 26.5 and 27.1 kg m^{-3} isopycnal surfaces yields a long-term mean volumetric subduction rate estimate of 56 Sv (1 Sv=10^6 m^3 s^{-1}). Vertical pumping induced by positive wind stress curl (Fig. 1c) is generally less than 50 m yr^{-1} (Fig. 2b), which contributes about 19 Sv (34%) to the total volumetric subduction rate. The remaining 37 Sv (66%) is accounted for by lateral induction, reflecting strong influence of the sloping winter MLDs (Fig. 2c).

The SAMW volumetric subduction rate (simply called the SAMW subduction rate below) varies from year to year (Fig. 3a). This year-to-year variability is predominantly quasi-biennial, particularly after 2009. To extract longer period variability, we apply a 3-year running mean filter to the time series, and the result shows an increasing trend of 0.73±0.65 Sv yr^{-1} at 95% confidence in the annual subduction rate. This increasing trend is consistent with but somewhat smaller than the earlier estimate (1.3 Sv yr^{-1}) based on model outputs for the Antarctic Circumpolar Current region during 1976-2006 (Liu and Huang, 2012). Given that the SAMW ventilation rate has remained relatively flat after 2010 (Fine et al., 2017), our estimate seems to be reasonable.

Using the Argo data from 2005 to 2015, Gao et al. (2018) recently reported a decade-long increase ($4.7\pm0.4\times10^4$ km^3 yr^{-1}) in the total SAMW volume. To explain this volume increase, we also calculate the linear trend of the SAMW subduction rate during 2005-2015. The increasing trend (1.04 ± 0.90 Sv yr^{-1}) during this period is notably higher than that (0.73 ± 0.65 Sv yr^{-1}) during 2005-2019. As such, nearly 70% of the observed increase in the total SAMW volume between 2005 and 2015 can be explained by the increasing trend of the SAMW subduction rate.

Close inspection of two subduction rate components (Eq. 1) indicates that lateral induction dominates the SAMW subduction rate variability (Fig. 3a). Vertical pumping remains little changed during the period of observation. As one can see from Eq. (1), changes in the MLDs and gyre circulation are processes governing the SAMW lateral induction. To identify the relative importance of these two processes, we also calculate the SAMW subduction rate and its components with (1) the long-term mean geostrophic velocities and temporally varying MLDs and (2) the long-term mean MLDs and temporally varying geostrophic velocities. The results show that temporally varying MLDs are the leading process modulating the SAMW subduction rate (Fig. 3b), though contributions from temporally varying geostrophic velocities are not negligible (Fig. 3c).

A quasi-biennial variability of the MLDs in the Sub-Antarctic Zone was recently reported by Lu et al. (2018) using the Argo data. To confirm this earlier result, we examine the time-longitude variability of the MLD averaged within the surface density range between 26.5 and 27.1 kg m^{-3} (Fig. 4a). As expected, the quasi-biennial variability of the MLDs is markedly evident across the Indian-Pacific Ocean. An eastward propagating signal is identified at a speed (~0.15 m s^{-1}) that is essentially the same as the surface current (Lu et al., 2018). Averaged over the entire southern hemisphere ocean within the surface density range between 26.5 and 27.1 kg m^{-3}, a quasi-biennial signal of the MLD is also visible (Fig. 4b). There are peak values occurring roughly every two years (say, 2007, 2009, 2011, 2013, etc.), which is generally consistent with the quasi-biennial variability of the SAMW subduction rate (Figs. 3a-b).

Approximately, 78% of the increasing trend of the SAMW subduction rate (Fig. 3a) is due to temporally varying MLDs (Fig. 3b), and about 22% is attributed to temporally varying geostrophic velocities (Fig. 3c) associated with the strengthening southern hemisphere super gyre (e.g., Roemmich, 2007; Qu et al., 2019). During the period of observation, the MLD averaged within the surface density range between 26.5 and 27.1 kg m^{-3} has deepened at 0.37±0.13 m yr^{-1} (Fig. 4b). The deepening of the MLDs directly contributes to the increasing trend of the SAMW subduction rate (Fig. 3b).

4. Subduction rate variability and Southern Annular Mode

From the analysis above, we have clearly demonstrated the importance of the MLDs in modulating the SAMW subduction rates. On interannual time scales, the quasi-biennial variability of the MLD largely contributes to the SAMW subduction rate variability, while its linear trend explains more than two thirds of the SAMW subduction rate increase (Fig. 3). Then, what controls the variability and trend of the MLDs? To address this question, we examine variability of the wind stress curl averaged over the SAMW subduction regions within the surface density range between 26.5 and 27.1 kg m^{-3} (Fig. 5a). In general, the time series of the wind stress curl shows a good correspondence with the MLDs (Fig. 4b). During the period of observation, the correlation between the two-time series reaches 0.72, satisfying the 95% confidence level, with the wind stress curl leading the MLDs by about 9 months. Closely related (r=0.76) to the wind stress curl in the SAMW subduction regions is the Ekman transport across the SAF (Fig. 5b). Ekman transport of the

Antarctic surface water directly contributes to the MLD variability in the SAMW formation regions (e.g., Sallee et al., 2008; Holte et al., 2012).

In addition to the Quasi-Biennial Oscillation of the tropical Pacific (Lu et al., 2018), we also emphasize the importance of the Southern Annular Mode (SAM) in driving the MLD variability. As shown in Fig. 5, both the wind stress curl in the SAMW subduction regions and the Ekman transport across the SAF are tightly linked to SAM. Measured as a normalized difference of sea level pressure between 40°S and 70°S (Thompson et al., 2000), SAM derived from the NCEP reanalysis product shows a large interannual variability with a notable quasi-biennial signal (Fig. 5c). Its correlation with the wind stress curl in the SAMW subduction regions and the Ekman transport across the SAF reaches 0.81 and 0.72, respectively, and both satisfy the 95% confidence level. Fluctuations of the westerly winds associated with SAM influence the northward Ekman transport across the SAF, also the wind stress curl and MLDs in the SAMW subduction regions, and eventually the SAMW subduction rate across the southern hemisphere ocean.

Motivated by the need to understand the warming trend of subsurface heat content in the extra-tropical southern hemisphere oceans (Gille, 2002; Roemmich et al., 2015), recent studies have noted the strengthening of the westerly winds (e.g., Qiu and Chen, 2006; Roemmich, 2007; Cai et al., 2011; van Sebille et al., 2012; Zhang and Qu, 2015; Gao et al., 2018; Qu et al., 2019). Here, we show that both the wind stress curl in the SAMW subduction regions (Fig. 5a) and the northward Ekman transport across the SAF (Fig. 5b) have increased during the past 15 years, with their rate reaching $5.6\pm9.8\times10^{-10}$ N m^{-3} yr^{-1} and 0.25 ± 0.14 Sv yr^{-1} at 95% confidence, respectively. These trends are closely related to the SAM (Fig. 5c). The SAM has experienced a notably increasing trend over the past decades (e.g., Thompson et al., 2000; Marshall, 2003; Wang et al., 2014; Qu et al., 2019), and this trend continues during the Argo period (Fig. 5c).

Sea surface density averaged in the SAMW subduction regions within the surface density range between 26.5 and 27.1 kg m^{-3} has slightly decreased at a rate of $-0.8\pm0.4\times10^{-3}$ kg m^{-3} yr^{-1} during the period of observation (Fig. 5d). This decreasing trend in surface density is largely due to surface warming ($0.7\pm0.7\times10^{-2}$ °C yr^{-1}) (Fig. 5e), while contribution of increasing sea surface salinity ($0.6\pm0.9\times10^{-3}$ psu yr^{-1}) is relatively minor (Fig. 5f). Decreasing sea surface density suggests that the increasing trend of the MLDs in the SAMW subduction regions cannot be accounted for by surface buoyancy fluxes, which is consistent with the earlier work of Gao et al. (2018). We therefore conclude that across the southern hemisphere ocean the trend of increasing wind stress curl associated with the strengthening westerly winds is primarily responsible for the deepening MLDs in the SAMW subduction regions. Consequently, the SAMW subduction rates across the southern hemisphere ocean have increased and should continue to increase, despite large differences between the three southern subtropical oceans (e.g., Lu et al., 2018; Meijers et al., 2019; Hong et al., 2020). The enhanced subduction of warmer surface water may directly contribute to the previously reported subsurface heat gain in the mid- to high-latitude southern hemisphere ocean.

5. Concluding remarks

This study has revealed a quasi-biennial variability in the SAMW subduction rates across the southern hemisphere ocean. Following earlier studies of the MLDs (Lu et al., 2018), we show that the quasi-biennial variability of the SAMW subduction rates is mostly due to variability of the MLDs. Similar quasi-biennial signals are also seen in wind stress curl over the SAMW subduction regions and Ekman transport across the SAF, both of which are tightly linked to the SAM. This suggests that fluctuations of the westerly winds in the mid- to high-latitudes of the southern hemisphere ocean play a critical role in generating the observed quasi-biennial variability of the MLDs and consequently the SAMW subduction rates.

It has been recognized that the thickening and deepening of the SAMW explain a large portion of the subsurface (0-2000m) heat gain in the extra-tropical southern hemisphere ocean (e.g., Roemmich et al., 2015; Gao et al., 2018). Here, we show that the SAMW subduction rate across the southern hemisphere ocean, with a long-term mean value of 56 Sv, has increased over the past 15 years. Nearly 70% of the observed increase in the total SAMW volume between 2005 and 2015 can be accounted for by the increasing SAMW subduction rates. Enhanced westerly winds associated with an increasing SAM directly contribute to the deepening of the MLDs, the strengthening of the subtropical gyres (Ridgeway and Dunn, 2007; Roemmich, 2007; Qu et al., 2019), the increasing of the SAMW subduction rates, and eventually the warming of the subsurface layers in the extra-tropical southern hemisphere ocean.

Acknowledgements:

This study was supported by NSF through grants 1829809 and 1829824. S. Gao was supported by the National Natural Science Foundation of China through grants 41676009. The Argo data were collected and made freely available by the international Argo Program and the national programs that contribute to it. The gridded Argo data product was downloaded at http://apdrc.soest.hawaii.edu/, and the NCEP Reanalysis wind product was downloaded at https://www.esrl.noaa.gov/psd/data/gridded/data.ncep.reanalysis.surfaceflux.html/. The authors are grateful to L. Talley for useful discussion on the topic.

References

Bindoff, N. L., and T. J. McDougall (2000), Decadal changes along an Indian Ocean section at 328S and their interpretation. J. Phys. Oceanogr., 30, 1207–1222.

Bryden, H. L., E. L. McDonagh, and B. A. King (2003), Changes in ocean water mass properties: Oscillations or trends. Science, 300, 2086–2088.

Cai, W., A. Sullivan, and T. Cowan (2011), Interactions of ENSO, the IOD, and the SAM in CMIP3 Models, J. Clim., 24(6), 1688–1704, doi: 10.1175/2010JCLI3744.1.

de Boyer Monte´gut, C., G. Madec, A. S. Fischer, A. Lazar, and D. Iudicone (2004), Mixed layer depth over the global ocean: An examination of profile data and a profile-based climatology, J. Geophys. Res., 109, C12003, doi:10.1029/2004JC002378.

Fine, R.A. (1993), Circulation of Antarctic Intermediate Water in the Indian Ocean. Deep-Sea Res., 40, 2021-2042.

Fine, R. A. (2011), Observations of CFCs and SF_6 as ocean tracers, Annu. Rev. Mar. Sci., 3, 173–195.

Fine, R. A., S. Peacock, M. E. Maltrud, and F. O. Bryan (2017), A new look at ocean ventilation time scales and their uncertainties, J. Geophys. Res. Oceans, 122, 3771–3798, doi:10.1002/2016JC012529

Gao L, Rintoul SR, Yu W (2018), Recent wind-driven change in Subantarctic Mode Water and its impact on ocean heat storage. Nat Clim Chang 8:58–63. doi: 10.1038/s41558-017-0022-8

Gille, S. T. (2002), Warming of the Southern Ocean since the 1950s. Science, 295, 1275–1277.

Hanawa, K. and L.D. Talley (2001), Mode Waters, In Ocean Circulation and Climate, G. Siedler and J. Church (eds.), Intl. Geophysics Series, Academic Press, 373-386.

Hartin, C.A., R. A. Fine, B. M. Sloyan, L. D. Talley, T. K. Chereskin, J. Happell (2011), Formation rates of Subantarctic Mode Water and Antarctic Intermediate Water within the South Pacific. Deep-Sea Res. I, 58, 524-534.

Holte JW, Talley LD, Chereskin TK, Sloyan BM (2012), The role of air-sea fluxes in Subantarctic Mode Water formation. J Geophys. Res. 117:1–17. doi: 10.1029/2011JC007798.

Hong, Y., Du, Y., Qu, T., Zhang, Y., & Cai, W. (2020), Variability of the subantarctic mode water volume in the South Indian Ocean during 2004–2018. Geophysical Research Letters, 47, e2020GL087830. https://doi.org/10.1029/2020GL087830

Huang, R. X., and B. Qiu (1998), The structure of the wind-driven circulation in the subtropical South Pacific Ocean, J. Phys. Oceanogr., 28, 1173-1186.

Kalnay, E., M. Kanamitsu, R. Kistler, W. Collins, D. Deaven, L. Gandin, M. Iredell, S. Saha, G. White, J. Woollen, Y. Zhu, M. Chelliah, W. Ebisuzaki, W. Higgins, J. Janowiak, K. C. Mo, C. Ropelewski, J. Wang, A. Leetmaa, R. Reynolds, R. Jenne, and D. Joseph (1996), The NCEP/NCAR 40-Year Re- analysis Project. Bull. Amer. Meteor. Soc., 77, 437–471, doi:10.1175/ 1520-0477(1996)077, 0437:TNYRP.2.0.CO;2.

Kara, A. B., P. A. Rochford, and H. E. Hurlburt (2000), An optimal definition for ocean mixed layer depth, J. Geophys. Res., 105, 16,803–16,821.

Kolodziejczyk, N., W. Llovel, and E. Portela (2019), Interannual variability of upper ocean water masses as inferred from Argo Array. Journal of Geophysical Research,124,6067–6085. https://doi.org/10.1029/2018JC014866

Liu, L. L., and R. X. Huang (2012), The Global Subduction/Obduction Rates: Their Interannual and Decadal Variability, J. Climate, 25, 1096-1115.

Llovel, W., and L. Terray (2016). Observed southern upper-ocean warming over 2005–2014 and associated mechanisms. Environ. Res. Lett., 11, 124023. doi:10.1088/1748-9326/11/12/124023

Lu, Y., L. D. Talley, I. Cerovecki, S.-P. Xie, M. R. Mazloff, S. Gille, Q. Liu (2018), Interannual variations and trend of Southern Ocean deep mixed layers and Sub-Antarctic mode water based on Argo data: patterns and mechanisms, 2018 AGU Fall Meeting Abstract (OS31H-1889).

Lukas, R. and E. Lindstrom (1991), The mixed layer of the western equatorial Pacific Ocean, J. Geophys. Res., 96, 3343-3358.

Marshall, G. J. (2003). Trends in the Southern Annular Mode from Observations and Reanalyses. J. Climate, 16, 4134–4143.

McCartney, M. S. (1977), Subantarctic Mode Water. A Voyage of Discovery: George Deacon 70th Anniversary Volume, M. V. Angel, Ed., Pergamon Press, 103-119.

McDonagh, E. L., H. L. Bryden, B. A. King, R. J. Saunders, S. A. Cunningham, and R. Marsh (2005), Decadal changes in the south Indian Ocean thermocline. J. Climate, 18, 1575–1590.

Meijers, A. J. S., Cerovečki, I., King, B. A., & Tamsitt, V. (2019). A see-saw in Pacific Subantarctic Mode Water formation driven by atmospheric modes. Geophysical Research Letters, 46, 13,152–13,160. https://doi.org/10.1029/2019GL085280.

Orsi, A., I. T. Whitworth, and J. W. D. Nowlin (1995), On the meridional extent and fronts of the Antarctic Circumpolar Current. Deep Sea Res. 42, 641–673.

Portela, E., N. Kolodziejczyk, C. Maes, Thierry Virginie (2020), Interior Water-Mass Variability in the Southern Hemisphere Oceans during the last decade. J. Phys. Oceanogr., 50(2), 361-381. https://doi.org/10.1175/JPO-D-19-0128.1.

Qiu, B., and R. X. Huang (1995), Ventilation of the North Atlantic and North Pacific: Subduction versus Obduction. J. Phys. Oceanogr., 25, 2374-2390.

Qiu, B. and S. Chen (2006), Decadal variability in the formation of the North Pacific Subtropical Mode Water: Oceanic versus atmospheric Control, J. Phys. Oceanogr., *36*, 1365-1380.

Qu, T., S.-P. Xie, H. Mitsudera, and A. Ishida (2002), Subduction of the North Pacific mode waters in a global high-resolution GCM, J. Phys. Oceanogr., *32*, 746-763.

Qu, T., S. Gao, I. Fukumori, R. A. Fine, and E. J. Lindstrom (2008), The subduction of South Pacific waters, Geophys. Res. Lett., 35, L02610, doi:10.1029/2007GL032605.

Qu, T., I. Fukumori, and R. A. Fine (2019), Spin-up of the Southern Hemisphere Super-Gyre, J. Geophys. Res., 124, https://doi.org/10.1029/2018JC014391.

Ridgway, K. R. and J. R., Dunn (2007), Observational evidence for a Southern Hemisphere oceanic supergyre. Geophys. Res. Lett. 34, L13612.

Roemmich, D., J. (2007), Super spin in the southern seas, Nature, Vol. 449, 34-35.

Roemmich, D., J. Church, J. Gilson, D. Monselesan, P. Sutton, and S. Wijffels (2015), Unabated planetary warming and its ocean structure since 2006. Nat. Clim. Change 5, 240–245.

Sabine CL, Feely RA, Gruber N, et al (2004), The oceanic sink for anthropogenic CO2. Science (80-) 305:367–371. doi: 10.1126/science.1097403

Sallée, J. B., Morrow, and K. Speer (2008), Eddy heat diffusion and Subantarctic Mode Water formation. Geophys. Res. Lett., 35, L05607.

Sallée, J. B., (2018), Southern Ocean warming. Oceanography, 31(2): 52-62, https://doi.org/10.5670/oceanog.2018.215.

Speich, S., B. Blanke, P. de Vries, S. Drijfhout, K. Doos, A. Ganachaud, and R. Marsh (2002), Tasman leakage: A new route in the global ocean conveyor belt, Geophys. Res. Lett., 29, doi:10.1029/2001GL014586.

Sprintal, J., and M. Tomczak (1992), Evidence of the barrier layer in the surface layer of the tropics, J. Geophys. Res., 97, 7305– 7316.

Talley, L. D., R.A. Feely, B.M. Sloyan, R. Wanninkhof, M.O. Baringer, J.L. Bullister, C.A. Carlson, S.C. Doney, R.A. Fine, E. Firing, N. Gruber, D.A. Hansell, M. Ishii, G.C. Johnson, K. Katsumata, R.M. Key, M. Kramp, C. Langdon, A.M. Macdonald, J.T. Mathis, E.L. McDonagh, S. Mecking, F.J. Millero, C.W. Mordy, T. Nakano, C.L. Sabine, W.M. Smethie, J.H. Swift, T. Tanhua, A.M. Thurnherr, M.J. Warner, and J.-Z. Zhang (2016), Changes in ocean heat, carbon content, ventilation: A review of the first decade Go-SHIP global repeat hydrography, Annu. Rev. Mar. Sci., 185–215.

Tanhua, T., D. W. Waugh, and J. L. Bullister (2013), Estimating changes in ocean ventilation from early 1990s CFC-12 and late 2000s SF6 measurements, Geophys. Res. Lett., 40, 927–932, doi:10.1002/grl.50251.

Thompson, D., J. Wallace, and G. Hegerl (2000), Annular modes in the extratropical circulation. Part II: Trends. J. Clim., 13, 1018–1036.

van Sebille, E., M. H. England, J. D. Zika, and B. M. Sloyan (2012), Tasman leakage in a fine-resolution ocean model, Geophys. Res. Lett., 39, L06601, doi:10.1029/2012GL051004.

Wang, G., W. Cai, and A. Purich (2014), Trends in Southern hemisphere wind-driven circulation in CIMIPs models over the 21st century: Ozone recovery versus greenhouse forcing. J. Geophys. Res. Oceans, 119, 2974–2986, doi:1002/2013JC009589.

Waugh, D. W., T. M. Hall, and T. W. N. Haine (2003), Relationships among tracer ages, J. Geophys. Res., 108(C5), 3138, doi:10.1029/2002JC001325.

Willey, D. A., Fine, R.A., Sonnerup, R.E., Bullister, J.L., Smethie Jr., W.M., Warner, M.J. (2004), Global oceanic chlorofluorocarbon inventory. Geophys. Res. Lett. 31, L01303 1–4.

Williams, R. G, M. Spall, and J. C. Marshall (1995), Does Stommel's mixed layer ''demon'' work? J. Phys. Oceanogr., 25, 3089–3102.

Woods, J. D. (1985), The physics of pycnocline ventilation. Coupled Ocean–Atmosphere Models, J. C. J. Nihoul, Ed., Elsevier Science, 543–590.

Zhang, L., and T. Qu (2015), Low frequency variability of the South Pacific Subtropical Gyre as seen from satellite altimetry and Argo, J. Phys. Oceanogr., 45, 3083–3098. doi: http://dx.doi.org/10.1175/JPO-D-15-0026.1.

Figure Captions

Figure 1 Long-term (2005-2019) mean characteristics of the region studied: a) sea surface temperature (˚C), b) sea surface salinity (psu), c) wind stress (vectors, unit: N m^{-2}) and its curl (color, unit: 10^{-7} N m^{-3}), and d) winter (September) mixed layer depth (m) in the southern hemisphere ocean between 20˚S and 60˚S. White contours indicate the winter (September) sea surface density (kg m^{-3}). The red solid lines indicate the location of the mean Subtropical and Sub-Antarctic Fronts (Orsi et al., 1995), and positive values in c) correspond to downward Ekman pumping.

Figure 2 Spatial distribution of annual subduction rate (m yr^{-1}) and its components within the surface density range 26.5-27.1 kg m^{-3} averaged over the period 2005-2019 from Argo. Negative values, which by definition are interpreted as zero annual subduction rates, are not shown. The black contours indicate the winter sea surface density (kg m^{-3}), and the red solid lines show the location of the mean Sub-Antarctic Front.

Figure 3 a) Variability and trend of volumetric annual subduction rate (Sv) of the SAMW and its components within the surface density range 26.5-27.1 kg m^{-3}, b) Same as a) except using climatological ocean circulation and temporally varying mixed layer depth, and c) Same as a) except using climatological mixed layer depth and temporally varying ocean circulation. The annual subduction rate filtered by a 3-year running mean filter (blue dashed) and its trend (green) are also included. The long-term (2005-2019) mean values have been removed before plotting.

Figure 4 Time-longitude variability of the MLD averaged within the surface density range between 26.5 and 27.1 kg m^{-3}, and b) temporal variability of the MLD averaged over the entire SAMW subduction regions between the 26.5 and 27.1 kg m^{-3} isopycnal surfaces. A 13-

month low-pass filter is applied and the long-term mean value of 83 m is subtracted before plotting in b). The red solid line in b) shows the linear trend of the regionally averaged MLD.

Figure 5 Variability and trend of a) wind stress curl, b) Ekman transport across the mean SAF, c) SAM index, d) sea surface density, e) sea surface temperature, and f) sea surface salinity normalized by their respective standard deviations. A 13-month low-pass filter is applied before plotting, and all the time series except for b) and c) are averaged over the SAMW subduction regions within the surface density range 26.5-27.1 kg m^{-3}.

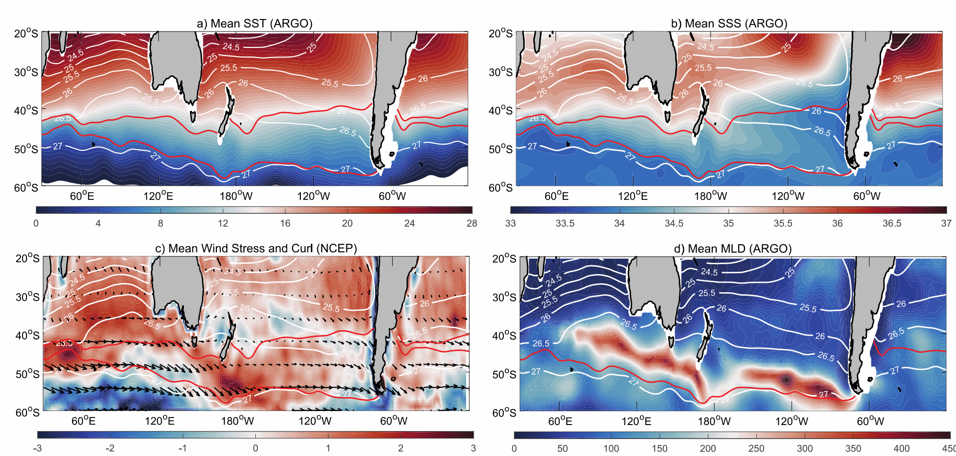

Figure 1 Long-term (2005-2019) mean characteristics of the region studied: a) sea surface temperature (°C), b) sea surface salinity (psu), c) wind stress (vectors, unit: N m^{-2}) and its curl (color, unit: 10^{-7} N m^{-3}), and d) winter (September) mixed layer depth (m) in the southern hemisphere ocean between 20°S and 60°S. White contours indicate the winter (September) sea surface density (kg m^{-3}). The red solid lines indicate the locations of the mean Subtropical and Sub-Antarctic Fronts (Orsi et al., 1995), and positive values in c) correspond to downward Ekman pumping.

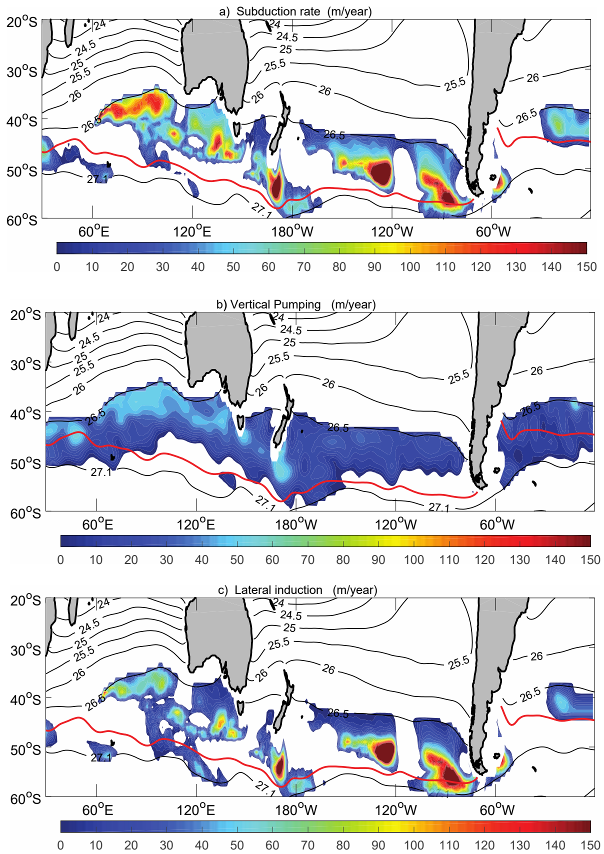

Figure 2 Spatial distribution of annual subduction rate (m yr^{-1}) and its components within the surface density range 26.5-27.1 kg m^{-3} averaged over the period 2005-2019 from Argo. Negative values, which by definition are interpreted as zero annual subduction rates, are not shown. The black contours indicate the winter sea surface density (kg m^{-3}), and the red solid lines show the location of the mean Sub-Antarctic Front.

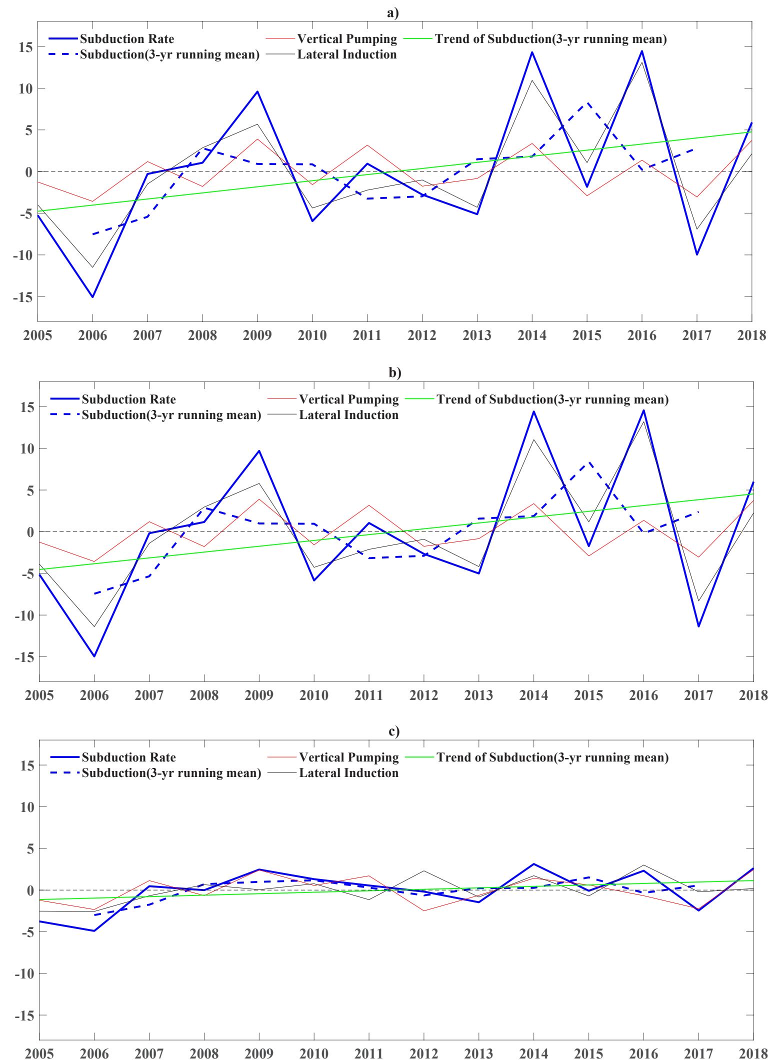

Figure 3 a) Variability and trend of volumetric annual subduction rate (Sv) of the SAMW and its components within the surface density range 26.5-27.1 kg m^{-3}, b) Same as a) except using climatological ocean circulation and temporally varying mixed layer depth, and c) Same as a) except using climatological mixed layer depth and temporally varying ocean circulation. The annual subduction rate filtered by a 3-year running mean filter (blue dashed) and its trend (green) are also included. The long-term (2005-2019) mean values have been removed before plotting.

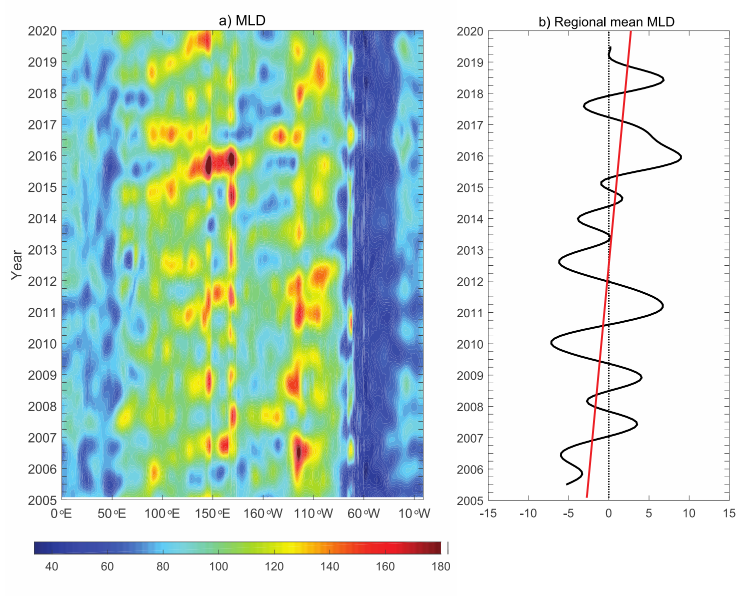

Figure 4 Time-longitude variability of the MLDs averaged within the surface density range between 26.5 and 27.1 kg m^{-3}, and b) temporal variability of the MLDs averaged over the entire SAMW subduction regions between the 26.5 and 27.1 kg m^{-3} isopycnal surfaces. A 13-month low-pass filter is applied and the long-term mean value of 83 m is subtracted before plotting in b). The red solid line in b) shows the linear trend of the regionally averaged MLDs.

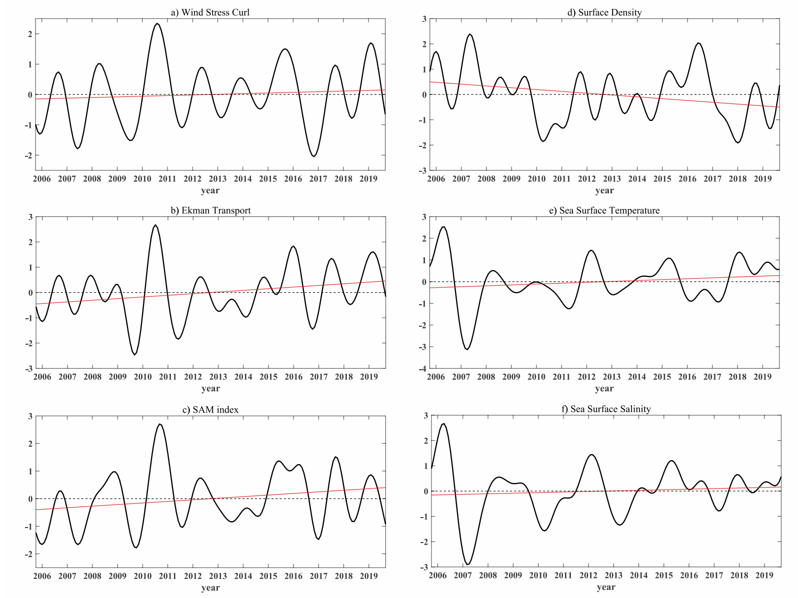

Figure 5 Variability and trend of a) wind stress curl, b) Ekman transport across the mean SAF, c) SAM index, d) sea surface density, e) sea surface temperature, and f) sea surface salinity normalized by their respective standard deviations. A 13-month low-pass filter is applied before plotting, and all the time series except for b) and c) are averaged over the SAMW subduction regions within the surface density range 26.5-27.1 kg m^{-3}.